

# A Manually Reconfigurable Reflective Spatial Sound Modulator for Ultrasonic Waves in Air

Jordi Prat-Camps, Giorgos Christopoulos, James Hardwick,\* and Sriram Subramanian

Precise control of ultrasonic acoustic waves with frequencies  $f \gtrsim 20$  kHz is useful in a range of applications from ultrasonic scanners to nondestructive testing and consumer haptic devices. A spatial sound modulator (SSM) is the acoustic analogy to the spatial light modulator (SLM) in optics and is highly sought after by acoustics researchers. A spatial sound modulator is constrained by very distinct practical conditions. Namely, it must be a reconfigurable device which modulates sound arbitrarily from a decoupled source. Here a reflective phase modulating device is realized, whose local units can be tuned to imprint a phase signature to an incoming wave. It is manually reconfigurable and consists of 1024 rigidly ended square waveguides with sliding bottom surfaces to provide variable phase delays. Experiments demonstrate the ability of this device to focus ultrasonic waves in air at different points in space, generate accurate pressure landscapes, and perform multiplane holography. Moreover, thanks to the subwavelength nature of the unit cells, this device outperforms state-of-the-art phased-array transducers of the same size in the quality and energy distribution of generated acoustic holographic images. These results pave the way for the construction of electronically controlled reflective SSMs.

There are myriad scientific and technological uses for sound waves beyond audible applications. In addition to the well-established field of medical ultrasound,<sup>[1,2]</sup> ultrasonic waves are used in parametric audio systems,<sup>[3]</sup> mid-air ultrasonic haptic devices,<sup>[4]</sup> personal health systems,<sup>[5,6]</sup> or contactless matter manipulation setups,<sup>[7]</sup> to name just a few examples. The development of novel devices and strategies to manipulate acoustic waves has, thus, an immense potential to improve existing technologies or to give rise to new ones.

At present, the control of ultrasonic wavefronts is attained following two different strategies. The main approach uses phased array transducers (PATs); a large ensemble of small speakers that

are individually driven and controlled.<sup>[8,9]</sup> By tuning the relative phase and amplitude of the signals driving different transducers, one can introduce precise delays between them and control the individual pressure level.<sup>[10–12]</sup> PATs can generate complex and fast-changing pressure landscapes, able to trap,<sup>[13]</sup> rotate, and move particles at high speeds.<sup>[14,15]</sup> In spite of their success, PATs suffer from some important limitations. Complex electronics with extreme timing requirements are used in order to maintain the synchronization, hampering the scalability. In addition to that, the transducers used in most mid-air ultrasonic PATs are bigger than the wavelength of the wave they generate,<sup>[10–15]</sup> which poses severe limitations to the accuracy of the acoustic landscapes they can produce.

The other existing approach is through fixed acoustic modulators,<sup>[16]</sup> namely, passive structures that locally modify the amplitude and/or the phase of a wave generated by some other source. This

approach encompasses the concept of acoustic metamaterials, whose exotic effective properties stem from their carefully engineered deep-subwavelength resonant microstructure.<sup>[17–19]</sup> Metamaterials have been shown to control waves in unusual ways,<sup>[20,21]</sup> providing perfect wave steering,<sup>[22]</sup> negative refraction, or focusing beyond the diffraction limit,<sup>[23]</sup> among many other examples. In the context of ultrasonic waves, a new level of control has been enabled with the recent development of holographic phase masks which can perform more complex operations than simple focusing. They have been able to create complex multiplane pressure landscapes,<sup>[24]</sup> move small particles along complex paths,<sup>[25]</sup> or even focus waves inside the human skull.<sup>[26]</sup> Made with affordable additive manufacturing technologies, their main limitation is their lack of reconfigurability; the phase masks are designed and 3D-printed to imprint a unique signature. To solve this, some proposals have combined arrays of transducers with specially designed static acoustic focusing lenses.<sup>[27]</sup> The versatility of the PAT complements the improved spatial resolution of the lens, allowing on-demand wave steering and focusing at different distances.

This hybrid control strategy is reminiscent of optical systems, in which the sources of light (lasers) and the control elements (spatial light modulators (SLMs)) are complemented with several static lenses. In the realm of optics, SLMs play a central role. They can imprint amplitude, phase, or polarization signatures to an existing beam.<sup>[28]</sup> They are reconfigurable,

Dr. J. Prat-Camps, G. Christopoulos, J. Hardwick, Prof. S. Subramanian  
Department of Informatics  
School of Engineering and Informatics  
University of Sussex  
Brighton BN1 9RH, UK  
E-mail: j.hardwick@sussex.ac.uk, J.A.H.1994@protonmail.com

 The ORCID identification number(s) for the author(s) of this article can be found under <https://doi.org/10.1002/admt.202000041>.

© 2020 The Authors. Published by WILEY-VCH Verlag GmbH & Co. KGaA, Weinheim. This is an open access article under the terms of the Creative Commons Attribution License, which permits use, distribution and reproduction in any medium, provided the original work is properly cited.

DOI: 10.1002/admt.202000041

fast, and extremely versatile. Crucially, a tool with analogous levels of control and versatility for ultrasound waves is yet to be developed. In the audible regime, a binary phase spatial sound modulator (SSM) has been proposed for shaping sound in closed reverberant environments.<sup>[29]</sup> However, the number of degrees of freedom present in cavities or closed rooms is high. The acoustic field is a combination of many standing wave modes not available in single-axis systems. Thus, alternative approaches to binary phase modulation must be considered.

In this work, we develop a manually reconfigurable reflective SSM and demonstrate an important step toward the construction of a true acoustic analog for SLMs. We go on to theoretically and experimentally demonstrate its ability to control the propagation of ultrasonic waves in air. The article is organized as follows. First, we present a discussion on the similarities and differences between optical and mid-air ultrasonic systems, paying special attention to the practical constraints that the latter impose. We discuss why the Nyquist rate of  $\lambda/2$  is the practical choice for the design for a metamaterial device that can accurately control ultrasonic waves. Next, we present the design and fabrication of a reconfigurable, reflective SSM consisting of 1024 independent rigidly ended square waveguides of a side length of  $\lambda/2$  and a sliding bottom surface. We experimentally show how this device is able to focus waves at different positions and generate complex acoustic holographic images of higher quality compared to commercial PATs of the same total size. Finally, we show how a smaller handheld modulator with only 256 reflectors is still able to focus the waves at different points and create simple holographic images.

The propagation of single-frequency linear acoustic waves is governed by the Helmholtz equation,<sup>[30,31]</sup> which also describes the propagation of monochromatic electromagnetic waves.<sup>[32]</sup> This sets a clear parallelism between both phenomena, even though the underlying physical principles are entirely different. As a result, concepts like diffraction, holography, or interference apply to both systems in a similar manner. Building upon this parallelism, research in ultrasound control has been borrowing knowledge and concepts from the well-established field of optical systems. Yet, despite their similarities, these two domains show dramatic practical differences.

Most mid-air ultrasonic applications use frequencies around 40 kHz, with corresponding wavelengths of  $\lambda_s \approx 8.58$  mm in air (assuming the room temperature of 20 °C). The typical sources of coherent ultrasound are arrays of circular transducers,<sup>[4]</sup> each of them having an individual diameter of  $\varnothing \approx 10$  mm  $\approx 1.2\lambda_s$ . These 2D arrays usually contain 256 transducers distributed in a square lattice, resulting in a total side length of  $l \approx 170$  mm  $\approx 20\lambda_s$ . Application of these arrays for mid-air haptics or particle trapping typically targets distances no greater than 50 cm  $\approx 58\lambda_s$  as beyond this the acoustic pressure becomes too low. In addition to the energy absorption by the medium, the main reason for this fast decrease in pressure is the spreading of the ultrasonic “beam” as it radiates from the transducer in a conical shape. As a ballpark comparison, the prototypical source of coherent light, a HeNe laser ( $\lambda_l = 633$  nm), generates an extremely tight parallel beam with a diameter of  $\approx 1$  mm ( $\approx 1600\lambda_l$ ). With a divergence of 1–2 mrad, the beam diameter spreads to just  $\approx 3$  mm after a propagation of 1 m  $\approx 1.5 \times 10^6 \lambda_l$  and much more energy is retained in the far field.

Another important difference between optical and air–ultrasonic systems is the availability of lenses. Optical systems use sets of commercial focusing lenses to control and condition the beam. In such lenses, optical refraction implements various phase signatures with reasonably high transmission efficiency. Conversely, equivalent lenses for air–ultrasonic applications are scarce. The large impedance mismatch between the air and any other solid material makes it effectively impossible to create beam controlling devices from homogeneous materials. The solution to this problem is lenses made up of individually engineered structures (metamaterial lenses),<sup>[20,33]</sup> which introduce predefined phase delays while trying to minimize back reflections and losses.

The ultimate control elements in optical systems are SLMs. The concept encompasses different technologies<sup>[28]</sup> (like liquid crystals and digital micromirror devices), which can control the amplitude, phase, or polarization of incoming light. Models can be transmissive or reflective, but the key feature is their reconfigurability; they contain an array of elements (pixels) that can be individually and externally controlled. Current commercial SLMs contain big arrays of pixels (they even achieve 4K resolution<sup>[34]</sup>), and the pitch between them is typically larger than  $4\lambda$ . These devices are used in conjunction with a system of optical lenses so that the desired wavefront control is generally attained in the far field.

For our objective of creating a reconfigurable reflective SSM, the aforementioned differences between optical and mid-air ultrasonic systems need to be carefully considered. The absence of traditional lenses in the acoustic regime and the rapid decay of the pressure make it necessary to control the waves at much shorter distances than in optical SLMs. Apart from the total size (aperture) of the SSM, which is usually subject to practicality, the most critical design parameter is the pitch of the pixels, i.e., the distance between adjacent pixels or elements forming the SSM.

For the sake of simplicity, let us consider a 2D space  $(x, z)$ . Given a known pressure distribution  $p(x, z_1)$ , at one plane  $z = z_1$ , the propagation to a second plane  $z_2$  is given by the angular spectrum method.<sup>[31]</sup> This method is exact to the level of the Helmholtz equation and, in contrast to some approaches used in optical holography like Fresnel/Fraunhofer approximations,<sup>[35]</sup> it does not contain any assumption as to the distance between the planes or the angles of the wave components. The pressure in  $z_2$  is given by

$$p(x, z_2) = \text{IFT} \left[ \text{FT} [p(x, z_1)] e^{i\sqrt{k^2 - k_x^2} (z_2 - z_1)} \right] \quad (1)$$

where FT and IFT stand for “Fourier transform” and “inverse Fourier transform,” respectively,  $k_x$  is the conjugate variable of  $x$ , and  $k = 2\pi/\lambda$  (see the Supporting Information for details). For far-field propagation, that is  $(z_2 - z_1) \gg \lambda$ , the exponential function in Equation (1) behaves like a low-pass filter on  $p(x, z_1)$ , and only wave components with  $|k_x| \leq k$  (the so-called propagating waves) contribute to the formation of the pressure signal at  $z_2$ .<sup>[36]</sup> As a result,  $p(x, z_1)$  has a maximum bandwidth  $B = k$ , and, following the Nyquist theorem<sup>[37]</sup> can be perfectly reconstructed when sampled at a rate of  $\Delta_x < \frac{2\pi}{2B} = \frac{\lambda}{2}$  (see also

Equation (S12) in the Supporting Information). Undersampled signals will have a bandwidth of  $B' < B$ , in which frequencies larger than  $B'$  are aliased, leading to significant spectral distortions that will translate to artifacts in the propagated

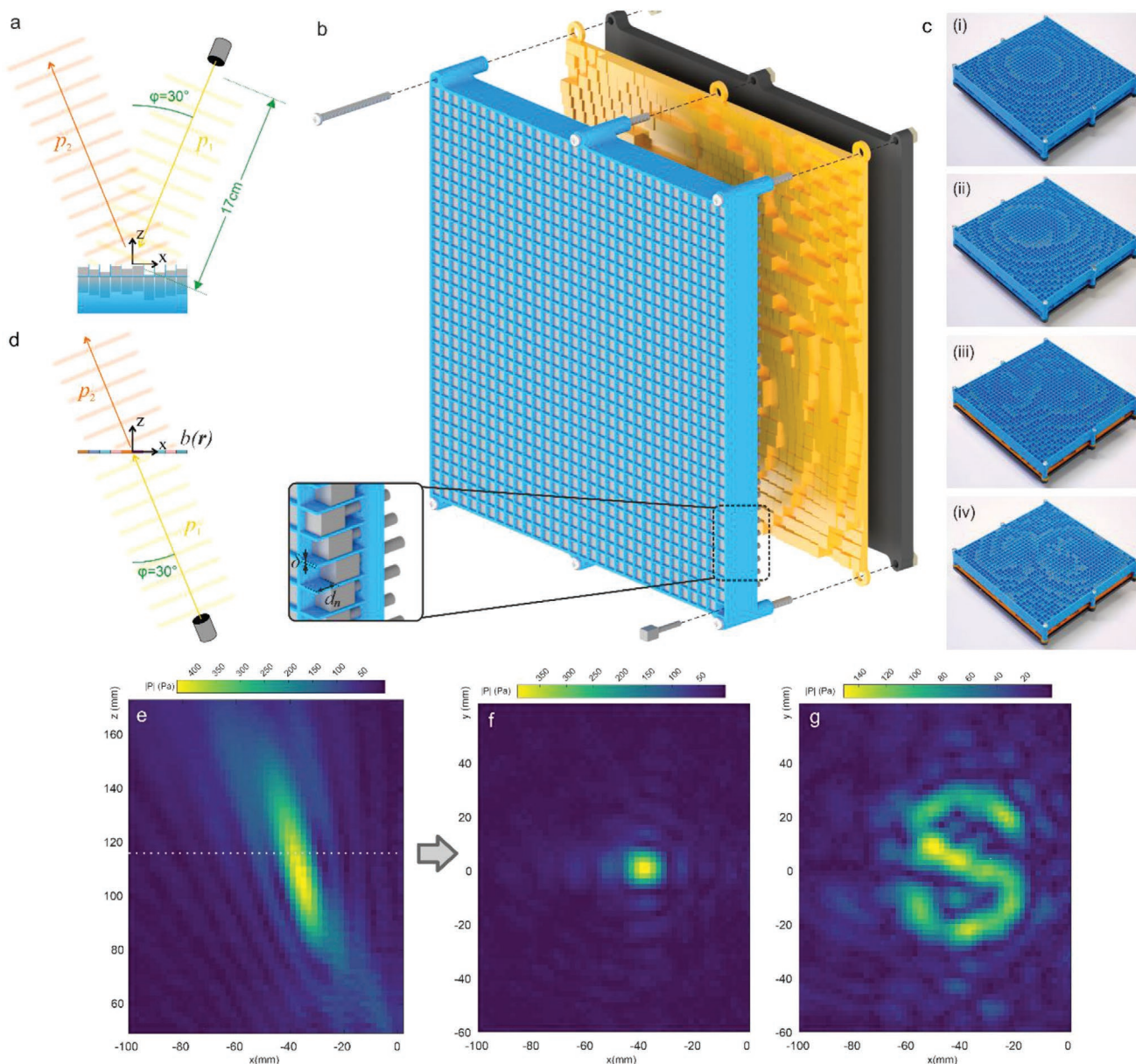


**Figure 1.** a) Sketch of the experimental setup. The transducer is shown in black gray. b) 3D exploded view of the device. The grid is shown in blue and the reflectors in gray. The displacements' template is shown in yellow. The inset shows a cross section of the SSM. c(i)–(iv)) Photographs of the SSM imprinting different phase maps. The different position of the pistons is visible. d) Sketch of the simplified transmissive model used to simulate the propagation of the waves after a phase signature  $b(r)$  is imprinted. e) Measurement of the reflected pressure in the  $xz$  plane ( $y = 0$ ) when a focal point phase signature is imprinted at  $(-37, 116)$  mm. f) Corresponding measurement in the  $xy$  plane ( $z = 13.5\lambda = 116$  mm). g) Same measurement as in panel (f) when the device is reconfigured to produce the image of the letter “S.”

acoustic field. Adhering to the Nyquist sampling theorem, pitches smaller than  $\lambda/2$  are redundant and do not reduce the aliasing effects any further.

In our experimental realization, the SSM reflects the incoming wave into the same half-space from which the wave is produced (see a sketch of the setup in **Figure 1a**); the space at the back is used to actuate the device. The SSM consists of a rectangular array of 1024 ( $32 \times 32$ ) rigidly ended square waveguides of side length  $\approx \lambda/2$  with a sliding bottom surface. Each of the waveguides introduces a phase delay,  $\phi_n$ , that can be approximated as  $\phi_n \approx 2kd_n$ , where  $d_n$  is the depth of the

waveguide (see the inset in **Figure 1b**). By sliding the bottom surface of the waveguide up and down, the phase delay can be continuously modified. In order to realize these variable-depth waveguides, the SSM is made of two parts: a rectangular grid with thin walls and a set of rectangular pistons with a cylindrical actuation pillar. Pistons are introduced in the grid, filling the rectangular spaces and resulting in a set of variable-length waveguides (see **Figure 1b**). Both the grid and the pistons are built using additive manufacturing techniques. The grid is 3D-printed in a fused-filament Flashforge Creator Pro printer using polylactide (PLA) plastic. The walls forming the grid

consist of single filament lines printed with a 0.4 mm diameter nozzle and a layer height of 0.2 mm. The resulting wall thickness is measured to be  $\delta = 0.47 \pm 0.02$  mm. Pistons are manufactured in a Formlabs Form 2 3D-printer using standard gray resin and a layer resolution of 100  $\mu\text{m}$ . They are printed with the rectangular section in an upward position, making use of a small support structure to achieve a flat and homogeneous finish on the top rectangular face. This face becomes the bottom sliding surface of the waveguides once the pistons are inserted into the grid.

The actuation of the pistons is done by pushing one of a set of prefabricated displacement templates onto the back of the SSM. These templates contain a map of displacements for each of the pistons and are manufactured using conventional fused-filament 3D printing (the vertical resolution of these maps is 0.2 mm). By exchanging these displacement maps, the SSM is reconfigured to imprint different phase signatures (see pictures of the SSM imprinting different phase maps in Figure 1c).

The experimental setup to test the SSMs consists of a single source of waves, an ultrasonic transducer (Murata MA40S4S) driven with a sinusoidal signal of frequency  $f = 40$  kHz. The transducer is located at a distance of  $\approx 17$  cm from the center of the SSM's surface (the origin of coordinates) and is oriented with an angle of  $30^\circ$  with respect to the normal as shown in Figure 1a. The acoustic pressure is measured at different planes of constant  $y$  or  $z$  using a pressure field microphone (B&K 4138-a-015; details in the Supporting Information). The microphone is attached to a 3D gantry that can move in XYZ directions. In order to separate the incoming wave,  $p_1$ , from the reflected one,  $p_2$ , we measure the complex incoming pressure  $p_1$  beforehand in absence of the SSM. Both the amplitude of the signal and the relative phase are recorded at each point. The SSM is then positioned carefully, and the total pressure ( $p_1 + p_2$ ) is measured. The subtraction of the two complex values results in the reflected pressure  $p_2$ .

We simulate the pressure reflected by the SSM using a simplified model, treating it as an ideal transmissive phase mask applying a complex signature,  $b(r)$ , to the incoming wave (Figure 1d). A mirror-symmetric image of the source is considered at  $z < 0$ , and the SSM is modeled as an array of  $32 \times 32$  square patches of size  $\lambda/2$ . All points within one of the squares (we denote the surface of the  $n$ th square as  $S_n$ ) introduce a constant phase delay,  $\phi_n$ , so that  $b(r) = 1e^{i\phi_n}$  for  $r \in S_n$ . For points outside the mask we set  $b(r) = 0$  to account for the finite size of the SSM in space.

**Focusing Waves:** Focusing is a simple and essential wave manipulation, used in mid-air haptic feedback<sup>[38–40]</sup> and trapping displays.<sup>[12,14,41]</sup> It is typically realized by imposing a phase signature, proportional to the distance between the source and the target focusing point, such that waves coming from different points reach the target with the same phase.<sup>[42]</sup> Following this geometric approach, the focusing signature at  $z_1$  is given by

$p(\mathbf{x}, z_1) = p_0 e^{-ik\sqrt{(x_0-x)^2 + (z_0-z_1)^2}}$ , where  $(x_0, z_0)$  are the coordinates of the target point and  $p_0$  is a reference pressure. The phase signature required to generate a focal point at the coordinates  $(x_0, y_0, z_0)$  is  $\phi(\mathbf{x}, \mathbf{y}) = -\phi_s(\mathbf{x}, \mathbf{y}) - ik\sqrt{(x_0-x)^2 + (y_0-y)^2 + z_0^2}$ . In this formula,  $\phi_s(\mathbf{x}, \mathbf{y})$ , corresponds to the phase of the incoming wave at the position  $(x, y, 0)$  in the SSM. We use the piston

model formula<sup>[31]</sup> to model the pressure emitted by the transducer and calculate  $\phi_s$ . The resulting phase signature is sampled at  $\lambda/2$  (the spacing between reflectors) and transformed into displacements, resulting in the actuation shown in Figure 1c(i). The reflected pressure measurements in Figure 1e,f demonstrate a clear focal point of pressure at the target location.

**Simple Holographic Images:** We create a complex acoustic pattern in the form of an acoustic holographic image.<sup>[24,43]</sup> The target shape is the letter “S” generated at the  $z = 13.5\lambda$  plane and centered at the same position as the previous focal point signature. In order to find the required phase map, we use a modified version of the iterative angular spectrum approach (IASA).<sup>[24,44]</sup> The algorithm (details in the Supporting Information) updates the target pressure distribution after some iterations over-weighting and underweighting the regions of the image where the pressure is lesser or greater than needed, respectively. In this way, the resulting images are more homogeneous and closer to their ideal shape. The resulting actuation of the SSM is shown in Figure 1c(ii) and the measurement of the reflected pressure in Figure 1g. The maximum value of pressure in the holographic image ( $\approx 150$  Pa), is significantly smaller than for the focusing case ( $\approx 350$  Pa), showing how the reflected pressure is spread over a wider area to generate the shape of the letter.

**Complex Holographic Images:** Next, we create a more complex holographic image containing the letters “U” and “S” (for University of Sussex) at  $z = 13.5\lambda$  (a sketch of the setup is shown in Figure 2a). We use the same algorithm to find the required actuation map (Figure 1c(iii)). The simulation and the measurement of reflected pressure (Figure 2b,c respectively) show a good agreement, demonstrating that our SSM can create complex acoustic holographic shapes. For comparison, we attempt to create the same image using a PAT of a similar size. It comprises an array of  $13 \times 13$  transducers (Murata MA40S4S) with a center-to-center spacing of 10.5 mm, and the same iterative algorithm is used to find the map of phases for each of the transducers. A sketch of the setup is shown in Figure 2d. The iterative method now converges to a solution in which both the amplitude and the phase of the transducers are controlled. The large ( $>\lambda$ ) distancing between the transducers introduces aliasing that translates to artifacts in the spatial domain. We use two evaluation metrics to quantify the results of Figures 2e and 3f; mean squared error (MSE) and structural similarity index (SSIM). MSE measures the average squares of the errors between an image and a reference image. SSIM combines an image's luminance, contrast, and structure to assess its perceptive quality over a reference image.<sup>[45]</sup> It is returned as a non-negative number that increases with similarity and reaches 1 for identical evaluation and reference (target) images. Formulas for the evaluation metrics can be found in the Supporting Information. As can be seen in Table 1, the SSM shows a smaller MSE and a higher perceptive quality compared to the PAT (see the Supporting Information for more information on data processing). To further emphasize this, we created the same image at a closer plane,  $z = 8\lambda$ . Reducing the distance to the target plane forces the system (SSM or PAT) to generate larger transverse wave components,  $(k_x, k_y)$ , which accentuates the aliasing. The SSM can produce an image very similar to the more distant previous one (compare Figure 2i,c). Conversely, when distance is reduced, the aliasing affecting the PAT worsens; the expected holographic image is

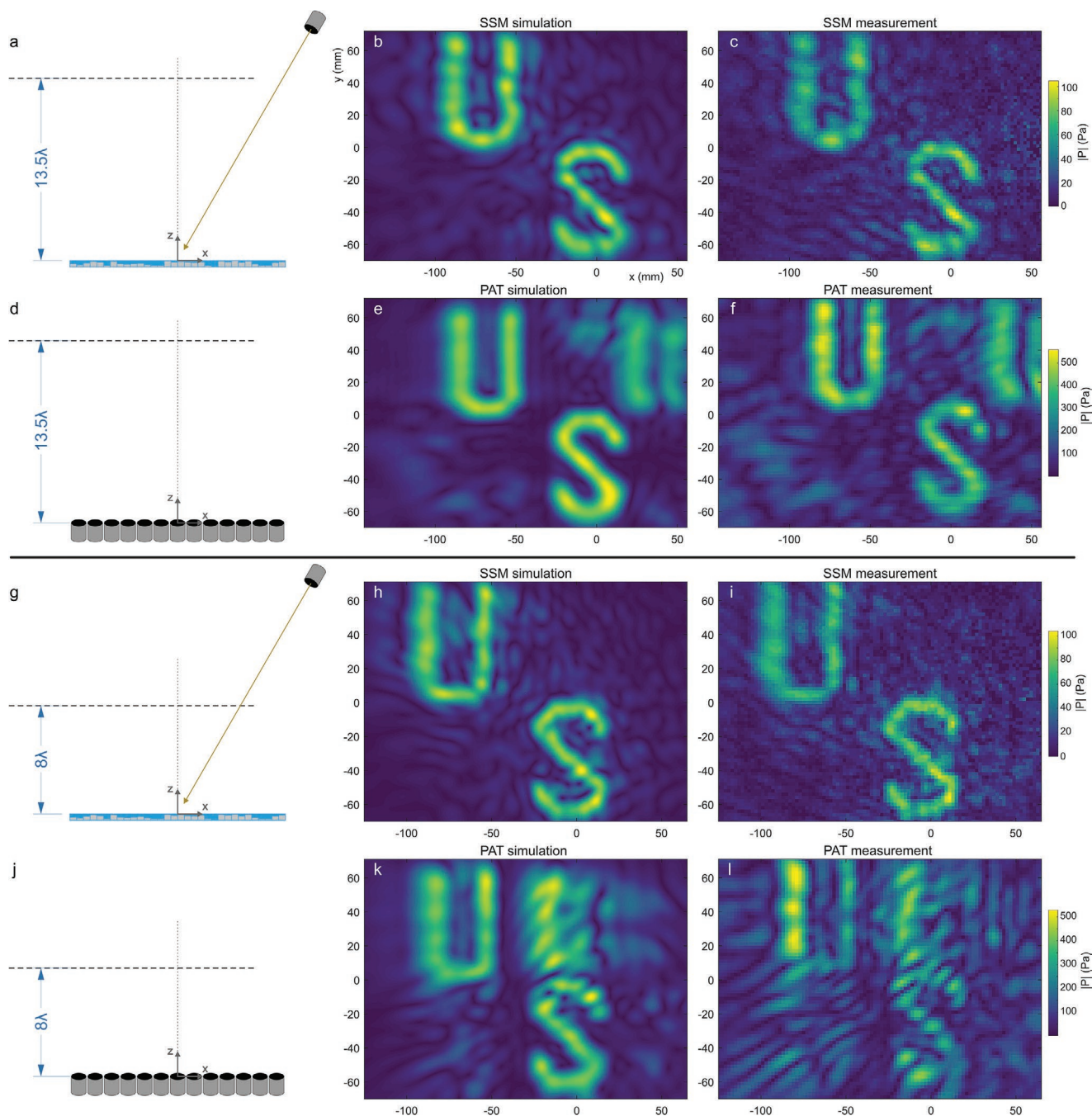


**Figure 2.** a) Sketch of the experimental setup for an SSM at the  $y = 0$  plane. The measurement plane is indicated with a dashed line and the SSM in blue/gray colors. b) Simulation and c) measurement of the pressure reflected by the SSM when generating a pressure landscape at the  $z = 13.5\lambda$  plane. d) Sketch of the experimental setup for a PAT at the  $y = 0$  plane. The target pressure map is the same as in panels (b) and (c). e) Simulation and f) measurement of the pressure generated by a PAT ( $13 \times 13$  transducers) at the  $z = 13.5\lambda$  plane. g–l) Analogous content, with the images now generated at the  $z = 8\lambda$  plane. All the simulations show normalized pressures, i.e.,  $|P|/P_{\max} \in [0,1]$ .

obviously distorted and artifacts have moved closer to the target image (Figure 2k,l). The difference in perceptive quality between the SSM and an equally sized PAT is larger, with the PAT also showing large MSE values (see Table 1). These results and evaluation demonstrate that our SSM can spread energy more accurately to form holographic images of higher quality than a PAT of the same size.

**Multiplane Holographic Images:** As a final example, we use our SSM to generate a multiplane holographic image.<sup>[21,24]</sup> In particular, we aim at generating the shape of two letters (letters “S” and “U” at two parallel planes ( $z = 7.5\lambda$  and  $15\lambda$ , respectively)). We use the same iterative algorithm with two target images to find the required actuation map (Figure 1c(iv)). Simulations shown in **Figure 3a,b** are in perfect agreement with the

**Table 1.** MSE and SSIM of simulations and measurements of our SSM and a same-sized PAT creating the holographic images of Figure 2.

Propagating distance	Acoustic field	MSE <sub>SSM</sub>	MSE <sub>PAT</sub>	SSIM <sub>SSM</sub>	SSIM <sub>PAT</sub>
13.5λ	Simulation	0.0330	0.0634	0.1617	0.1053
	Measurement	0.0355	0.0712	0.1508	0.1230
8λ	Simulation	0.0318	0.0809	0.1875	0.0974
	Measurement	0.0362	0.0793	0.1571	0.0858

corresponding measurements in Figure 3c,d. Extending the manipulation of ultrasound in 3D space has proven important for different applications, such as acoustophoretic 3D printing<sup>[46]</sup> and multiparticle ultrasound levitation.<sup>[12]</sup> Reconfigurable modulators can assist in these by providing faster parallel volumetric scanning.

The design concept of this device is such that the number of elements making it up can be scaled up or down to any number required, with the resolving power and complexity of formed holographic images changing accordingly. Our SSM containing 32 × 32 elements demonstrates good control abilities with a lateral size of ≈ 14 cm. We built a smaller handheld version of the SSM containing only 16 × 16 reflectors (see Figure 3h). As can be seen in the measurements of Figure 3e–g, it was still able to produce focal points at different positions, even though the peak pressure values (≈ 120 Pa) were significantly smaller than those generated with the larger version (≈ 350 Pa). This device was also reconfigured to produce a simple holographic image (compare simulation and measurement in Figure 3i,j, respectively) even though, in this case, the complexity of the

pressure landscape was greatly limited by its smaller number of elements. This can also be deduced from Table 2, where it is shown that the 16 × 16 SSM achieved larger MSEs and smaller SSIMs in both simulations and experiments. Finally, as the functionality of the device depends on elements of size λ/2, changing the operational frequency from 40 kHz would simply be a case of scaling the geometry of the device up or down by the same factor by which one scaled the frequency.

We have presented a phase-manipulating device for ultrasonic waves and demonstrated its ability for control with better accuracy than state-of-the-art phased arrays of transducers. Although our system utilizes a single ultrasound transducer with limited strength, our SSM could be used in combination with other sound sources that provide stronger pressures to generate haptics and particle manipulation. The devices presented in this work require the manufacture and application of displacement templates to move the pistons to the correct positions, but we envision many ways in which one can create an electronically controlled actuation system. Liquid crystal displays use a multiplexing strategy to control an *n*-by-*m* array of crystals. In this way, one does not need a dedicated controller for every pixel but only one for each row and column. Similarly, one could envision an array of microstepper motors or miniature solenoid magnets (with sufficient interelement shielding) placed beneath each of the sliding reflectors and facilitating multiplexed control over each element in the metasurface individually. An approach akin to this was undertaken in recent work where a compact array of independently controlled electronic actuators was employed to supply haptic sensation to the skin in virtual reality.<sup>[47]</sup> An activated metamaterial SSM will continue to maintain many advantages over a

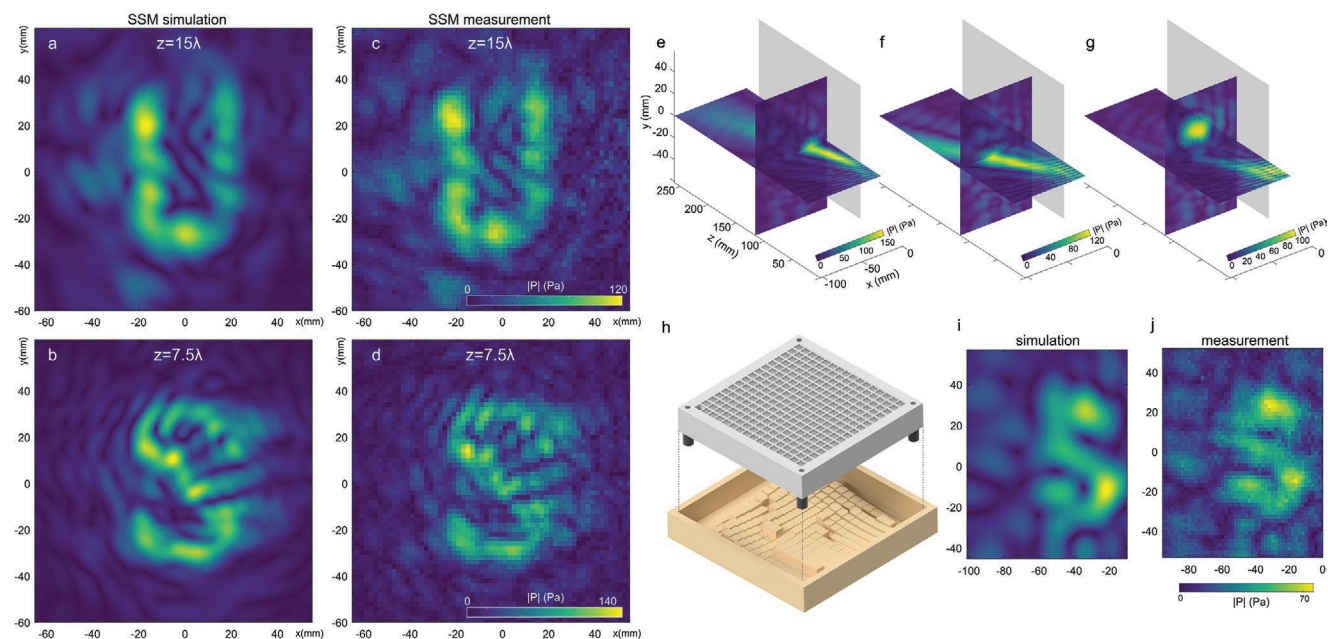


**Figure 3.** a,b) Simulations and c,d) the corresponding measurements of the pressure reflected by the SSM at two different planes (multiplane holographic image). Panels (a) and (c) correspond to  $z = 15\lambda$  and panels (b) and (d) to  $z = 7.5\lambda$ . e–g) Results obtained with a smaller SSM containing 256 reflectors and sketched in panel (h). e–g) Measurements of the *xz* and *xy* planes, when the small SSM is configured to focus the acoustic pressure at different points. In these measurements, a thin wall (shown in gray) was placed in the middle of the experiment to separate the incoming from the reflected waves. j) A simple image generated with this same SSM, in good agreement with i) the corresponding simulation. More details are given in the Supporting Information. a,b,i) All the simulations show normalized pressures ( $|P|/P_{\max}$ ).

**Table 2.** MSE and SSIM of simulations and measurements of a  $16 \times 16$  and  $32 \times 32$  SSM creating a holographic image of the letter “S”.

Propagating distance	Acoustic field	MSE <sub>16</sub>	MSE <sub>32</sub>	SSIM <sub>16</sub>	SSIM <sub>32</sub>
13.5λ	Simulation	0.0268	0.0135	0.1606	0.2653
	Measurement	0.0384	0.0151	0.1367	0.1664

PAT counterpart. First, the power requirements and level of electronic complexity for a PAT are significant as the transducers must act as the wave source and modulate both amplitude and phase simultaneously. By comparison, the activated metasurface we propose has a decoupled wave source (a significant saving in power consumption) and would only require actuation while the device switches between phase maps, remaining at rest in between generation of holographic images. Furthermore, PAT transducers must be updated with a speed determined by the operating frequency (40 kHz), such precision timing control can be difficult to perfect and would not be needed for the active SSM we propose, which can be controlled by comparatively simple multiplexing strategies. Another promising line of research is simultaneous control of both phase and amplitude. The inclusion of deep-subwavelength structures in the surface of reflectors could convert propagating waves into evanescent waves and produce on-demand attenuation of the amplitude. “Super-pixel” concepts comparable to this have been explored in optics,<sup>[48]</sup> and there have been similar ideas of encoding both amplitude and phase information into hologram generators stretching back as far as the 1960s and 70s.<sup>[49,50]</sup> The modulation of phase and amplitude simultaneously could improve even further the acoustic wave control already attained by our SSMs.

## Supporting Information

Supporting Information is available from the Wiley Online Library or from the author.

## Acknowledgements

This project received funding from the EU’s ERC Advanced Grant No. 787413. J.P.C. is funded by a Leverhulme Trust Early Career fellowship (ECF-2018-447). S.S. is funded by the Royal Academy of Engineering grant CIET1718-14.

## Conflict of Interest

The authors declare no conflict of interest.

## Keywords

metamaterials, spatial-sound-modulators, ultrasound

Received: January 17, 2020

Revised: April 29, 2020

Published online:

- [1] T. L. Szabo, *Diagnostic Ultrasound Imaging: Inside Out*, 2nd ed., Academic Press, Cambridge, MA 2014.
- [2] K. G. Baker, V. J. Robertson, F. A. Duck, *Phys. Ther.* **2001**, *81*, 1351.
- [3] Audio Spotlight by Holosonics—Focused Audio Technology, www.holosonics.com (accessed: November 2019).
- [4] Ultraleap: Digital worlds that feel human, www.ultraleap.com (accessed: June 2020).
- [5] Sustained Acoustic Medicine | ZetrOZ Systems, LLC | ZetrOZ Systems, www.zetroz.com (accessed: November 2019).
- [6] DFree—US site wearable bladder scanner for incontinence, www.dfreeus.biz (accessed: November 2019).
- [7] D. Foresti, M. Nabavi, M. Klingauf, A. Ferrari, D. Poulikakos, *Proc. Natl. Acad. Sci. USA* **2013**, *110*, 12549.
- [8] D. H. Turnbull, F. S. Foster, *IEEE Trans. Ultrason. Ferroelectr. Freq. Control* **1991**, *38*, 320.
- [9] S. C. Wooh, Y. Shi, *Ultrasonics* **1998**, *36*, 737.
- [10] A. Marzo, S. A. Seah, B. W. Drinkwater, D. R. Sahoo, B. Long, S. Subramanian, *Nat. Commun.* **2015**, *6*, 8661.
- [11] A. Marzo, A. Ghobrial, L. Cox, M. Caleap, A. Croxford, B. W. Drinkwater, *Appl. Phys. Lett.* **2017**, *110*, 014102.
- [12] A. Marzo, B. W. Drinkwater, *Proc. Natl. Acad. Sci. USA* **2019**, *116*, 84.
- [13] A. Marzo, M. Caleap, B. W. Drinkwater, *Phys. Rev. Lett.* **2018**, *120*, 044301.
- [14] R. Hirayama, D. Martinez Plasencia, N. Masuda, S. Subramanian, *Nature* **2019**, *575*, 320.
- [15] T. Fushimi, A. Marzo, B. W. Drinkwater, T. L. Hill, *Appl. Phys. Lett.* **2019**, *115*, 064101.
- [16] R. J. Lalonde, A. Worthington, J. W. Hunt, *IEEE Trans. Ultrason. Ferroelectr. Freq. Control* **1993**, *40*, 592.
- [17] Y. Xie, W. Wang, H. Chen, A. Konneker, B. I. Popa, S. A. Cummer, *Nat. Commun.* **2014**, *5*, 5553.
- [18] G. Ma, P. Sheng, *Sci. Adv.* **2016**, *2*, e1501595.
- [19] S. A. Cummer, J. Christensen, A. Alù, *Nat. Rev. Mater.* **2016**, *1*, 16001.
- [20] G. Memoli, M. Caleap, M. Asakawa, D. R. Sahoo, B. W. Drinkwater, S. Subramanian, *Nat. Commun.* **2017**, *8*, 14608.
- [21] Y. Zhu, J. Hu, X. Fan, J. Yang, B. Liang, X. Zhu, J. Cheng, *Nat. Commun.* **2018**, *9*, 1632.
- [22] A. Díaz-Rubio, S. A. Tretyakov, *Phys. Rev. B* **2017**, *96*, 125409.
- [23] N. Kaina, F. Lemoult, M. Fink, G. Lerosey, *Nature* **2015**, *525*, 77.
- [24] K. Melde, A. G. Mark, T. Qiu, P. Fischer, *Nature* **2016**, *537*, 518.
- [25] Z. Ma, A. W. Holle, K. Melde, T. Qiu, K. Poeppel, V. M. Kadiri, P. Fischer, *Adv. Mater.* **2020**, *32*, 1904181.
- [26] S. Jiménez-Gambín, N. Jiménez, J. M. Benlloch, F. Camarena, *Phys. Rev. Appl.* **2019**, *12*, 014016.
- [27] M. A. Norasikin, D. M. Plasencia, S. Polychronopoulos, G. Memoli, Y. Tokuda, S. Subramanian, in *UIST 2018: The 31st Annual ACM Symp. on User Interface Software and Technology* (Eds: P. Baudisch, A. Schmidt, A. Wilson), Association for Computing Machinery, New York, NY **2018**, pp. 247–259.
- [28] U. Efron, *Spatial Light Modulator Technology: Materials, Devices, and Applications*, CRC Press, Inc., Boca Raton, FL **1995**.
- [29] G. Ma, X. Fan, P. Sheng, M. Fink, *Proc. Natl. Acad. Sci. USA* **2018**, *115*, 6638.
- [30] H. Bruus, *Lab Chip* **2012**, *12*, 20.
- [31] E. G. Williams, *Fourier Acoustics*, Academic Press, Cambridge, MA **1999**.
- [32] L. Novotny, B. Hecht, *Principles of Nano-Optics*, Cambridge University Press, Cambridge **2009**.
- [33] G. Memoli, L. Chisari, J. P. Eccles, M. Caleap, B. W. Drinkwater, S. Subramanian, in *CHI’19: Proc. of the 2019 CHI Conf. on Human Factors in Computing Systems* (Eds: S. Brewster, G. Fitzpatrick, A. Cox, V. Kostakos), Association for Computing Machinery, New York, NY **2019**.

- [34] Forth Dimension Displays, <http://www.forthdd.com> (accessed: June 2020).
- [35] J. W. Goodman, *Introduction to Fourier Optics*, W. H. Freeman, New York, NY **2005**.
- [36] M. Karaman, M. O'Donnell, *IEEE Trans. Ultrason. Ferroelectr. Freq. Control* **1998**, *45*, 126.
- [37] H. Nyquist, *Trans. Am. Inst. Electr. Eng.* **1928**, *47*, 617.
- [38] D. Spelmezan, R. M. González, S. Subramanian, in *2016 IEEE Haptics Symp. (HAPTICS)*, (Eds: S. Choi, K. J. Kuchenbecker), IEEE, Piscataway, NJ **2016**.
- [39] T. Carter, S. A. Seah, B. Long, B. Drinkwater, S. Subramanian, in *UIST'13: Proc. of the 26th Annual ACM Symp. on User Interface Software and Technology* (Eds: S. Izadi, A. Quigley, I. Poupyrev, T. Igarashi), Association for Computing Machinery, New York, NY **2013**.
- [40] B. Long, S. A. Seah, T. Carter, S. Subramanian, *ACM Trans. Graph.* **2014**, *33*, 6.
- [41] S. Polychronopoulos, G. Memoli, *Sci. Rep.* **2020**, *10*, 4254.
- [42] Y. Li, G. Yu, B. Liang, X. Zou, G. Li, S. Cheng, J. Cheng, *Sci. Rep.* **2014**, *4*, 6830.
- [43] Y. Xie, C. Shen, W. Wang, J. Li, D. Suo, B. I. Popa, Y. Jing, S. A. Cummer, *Sci. Rep.* **2016**, *6*, 35437.
- [44] S. Mellin, G. Nordin, *Opt. Express* **2001**, *8*, 705.
- [45] Z. Wang, A. C. Bovik, H. R. Sheikh, E. P. Simoncelli, *IEEE Trans. Image Process.* **2004**, *13*, 600.
- [46] D. Foresti, K. T. Kroll, R. Amisshah, F. Sillani, K. A. Homan, D. Poulidakos, J. A. Lewis, *Sci. Adv.* **2018**, *4*, eaat1659.
- [47] X. Yu, Z. Xie, Y. Yu, J. Lee, A. Vazquez-Guardado, H. Luan, J. Ruban, X. Ning, A. Akhtar, D. Li, B. Ji, Y. Liu, R. Sun, J. Cao, Q. Huo, Y. Zhong, C. Lee, S. Kim, P. Gutruf, C. Zhang, Y. Xue, Q. Guo, A. Chempakasseril, P. Tian, W. Lu, J. Jeong, Y. Yu, J. Cornman, C. Tan, B. Kim, K. Lee, X. Feng, Y. Huang, J. A. Rogers, *Nature* **2019**, *575*, 473.
- [48] S. A. Goorden, J. Bertolotti, A. P. Mosk, *Opt. Express* **2014**, *22*, 17999.
- [49] B. R. Brown, A. W. Lohmann, *Appl. Opt.* **1966**, *5*, 967.
- [50] W.-H. Lee, *Appl. Opt.* **1979**, *18*, 3661.